ACS APPLIED NANO MATERIALS

www.acsanm.org Article

Electrocatalytic Studies of Coral-Shaped Samarium Stannate Nanoparticles for Selective Detection of Azathioprine in Biological Samples

Ramachandran Rajakumaran, Karuppaiah Balamurugan, Shen-Ming Chen,* Ramaraj Sukanya, and Carmel B. Breslin

Cite This: *ACS Appl. Nano Mater.* 2021, 4, 13048−13059 Read Online

ACCESS | Metrics & More | Article Recommendations | Supporting Information

ABSTRACT: An electrochemical sensor was developed based on the pyrochlore-type binary metal oxide samarium stannate nanoparticles ($Sm_2Sn_2O_7$ NPs). The $Sm_2Sn_2O_7$ NPs were prepared using the co-precipitation technique, and they were subjected to physiochemical characterizations such as X-ray diffraction (XRD), Raman spectroscopy, and X-ray photoelectron spectroscopy (XPS). The morphological and elemental information was interpreted by field-emission scanning electron microscopy (FESEM) and high-resolution transmission electron microscopy (HRTEM) analysis. The electrocatalytic sensing of the pharmaceutical drug azathioprine (AZN) was exhibited using cyclic voltammetry (CV) and differential pulse voltammetry (DPV) over the $Sm_2Sn_2O_7$/GCE (GCE - glassy carbon electrode). The $Sm_2Sn_2O_7$/GCE had high electrocatalytic behavior for AZN determination with a limit of detection of 4 nM and superior sensitivity of 0.27 μA μM^{-1} cm^{-2}, and it has a linear range from 0.01 to 948 μM. Furthermore, the $Sm_2Sn_2O_7$/GCE exhibited excellent selectivity, long-term storage stability, good repeatability, and reproducibility for AZN detection. Additionally, the $Sm_2Sn_2O_7$/GCE sensor possessed considerable importance for the sensing of AZN in biological fluids for practical applications. We believe that this pyrochlore-based $Sm_2Sn_2O_7$ NP electrocatalyst can act as a prospective electrode material for the electrochemical determination of AZN in clinical biological applications.

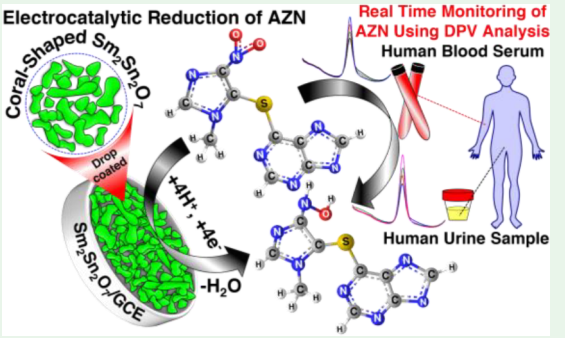

KEYWORDS: *pyrochlore oxide, samarium stannate nanoparticles, azathioprine detection, electrochemical sensor, biological samples*

1. INTRODUCTION

Bimetallic oxides have been extensively used in both fundamental and applied research, owing to their remarkable properties like high bulk conductivity, piezoelectricity, luminescence, and redox properties.[1−7] The pyrochlore oxides, which consist of trivalent (A^{3+}) and tetravalent (B^{4+}) cations with a structural formula of $A_2B_2O_7$, belong to the *Fd*3*m* space group containing two different oxygen compositions. They possess higher ionic/electronic conductivity, superior chemical and physical stability, and they have been extensively utilized as electrocatalysts for various electrochemical studies.[8] On the basis of their oxygen vacancies, the crystalline nature and chemical stability of pyrochlore oxides are altered by tuning their elemental ions in A or B sites. This combination of different vacancy A and B sites manipulates their electrocatalytic properties in different types of applications such as photocatalysts, anode materials for different electrochemical applications such as solid electrolyte fuel cells, ionic/electrical conductors, electrocatalysts for electrochemical sensors, and water splitting reactions.[9−14] Particularly, pyrochlore oxides with high metallic conductivity are attractive candidates for electrochemical sensing due to their fast charge transfer through the oxygen vacancies and higher structural stability. In that series, the rare earth (RE) pyrochlore stannate compounds ($RE_2Sn_2O_7$) have abundant surface oxygen sites, high chemical stability, and tunable crystal structural order. It is considered to be a low-cost effective catalyst, and it is widely employed for electrochemical sensing applications.[14] For example, the members of lanthanide stannate such as $La_2Sn_2O_7$,[15] $Dy_2Sn_2O_7$,[16] and $Pr_2Sn_2O_7$[17] are the most familiar electrocatalysts due to their significant properties like fast charge transferability, superior chemical stability, lower activation energy, ionic mobility, high melting point and have large surface area.[18] The spin−orbital coupling phenomenon in the RE oxides directly relates to the higher electronegativity and

Received: August 20, 2021
Accepted: November 18, 2021
Published: December 6, 2021

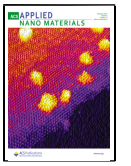

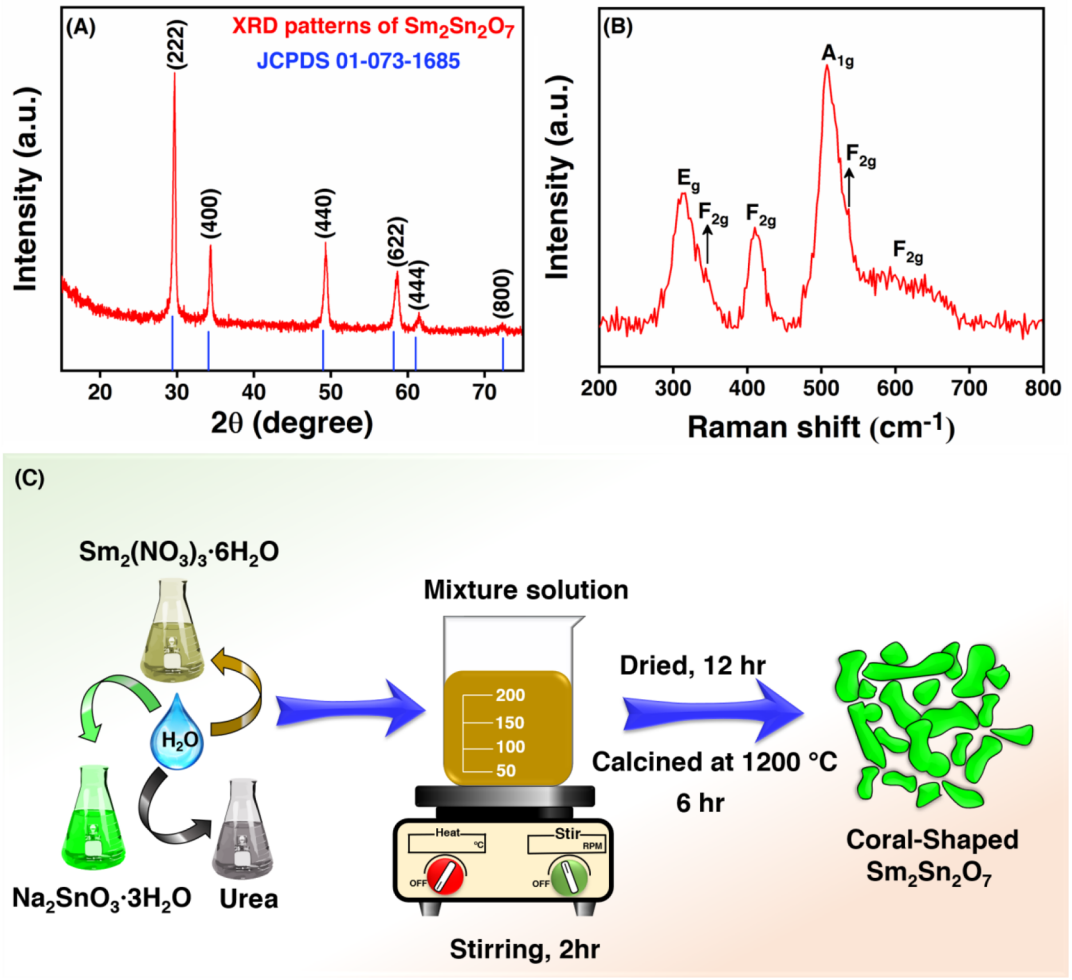

Figure 1. (A) XRD patterns and (B) Raman spectra of $Sm_2Sn_2O_7$. (C) Detailed co-precipitation method for the preparation of $Sm_2Sn_2O_7$.

basicity, thereby improving metal and analyte interaction during electrochemical sensing.[19] Hence, the history and defect chemistry of lanthanide stannate were already discussed in our previous article.[17] Samarium stannate ($Sm_2Sn_2O_7$), a new type of inorganic material that was used in the form of a sensing material in recent studies because of its abundant surface oxygen species, is an essential compound.[20] In addition to that, the Sm is an element with an ionic radius (1.08 Å) that exists in between those of europium (Eu) and yttrium (Y), which is also an important point for the enhanced electrochemical behavior of samarium-based compounds.[21] More deeply, the presence of Sm in stannate form will induce n-type conduction (7.29×10^{-10} Ω cm^{-1}), which increases the electronic conductivity associated with mixed different oxidation states (+2 and +3 states), which leads to their enhanced electrochemical properties.[20,22] For example, our group's previous article by Sukanya et al. proved that the combination of rare earth stannate oxide (CeO_2−SnO_2) should be a suitable electroactive material for electrochemical detection of the pharmaceutical drug mesalamine.[23] Followed by this, Rajakumaran et al. clearly discussed the electrochemical behavior of pyrochlore-type praseodymium stannate for the electrochemical sensing of a nitrofurazone drug in biological fluids.[17] Other than that, Duan et al. proved that the $Sm_2Sn_2O_7$ ceramic is a suitable material for the NO_2 sensing process.[20] On the basis of these studies, we believe that the unique behavior of Sm^{3+} ($4f^6$ $6s^2$) endows different band structures and mixed-valence states in nature, which will induce high electronic transport for improved electrochemical sensing phenomena.

Azathioprine (AZN) belongs to a class of purine base analogues, is used as an immunosuppressive antileukemic drug for organ transplantation (kidney or liver), and also acts as a medication route to prevent new organ transplant immunological rejections.[24] This drug is also used for the treatment of autoimmune health problems like inflammatory bowel disease, autoimmune and inflammatory disease, multiple sclerosis, and lupus erythematosus. However, this drug is converted into the form mercaptopurine, which interrupts the activity of human immune systems. Long-term usage of AZN will produce serious side effects such as bone marrow suppression, nausea, fatigue, hair loss, and rash, and it is the reason for the development of certain cancers like skin cancer, leukemia, and lymphoma.[25−27] Because of these effects, the usage of AZN drugs is limited to reduce the toxicity factor. On this account, it is important to use a supersensitive approach for the determination of the concentration of AZN in clinical approaches. For that, various techniques like chemiluminescence, surface-enhanced Raman spectroscopy, high-performance liquid chromatography, ^{1}H NMR spectroscopy, and capillary zone electrophoresis have been previously reported for AZN determination.[28−32] The aforementioned methods have a lot of disadvantages, namely, low selectivity, sample pretreatment, long time processing, and expensive cost, for the detection of AZN drugs. In recent times, the electrochemical

https://doi.org/10.1021/acsanm.1c02591
ACS Appl. Nano Mater. 2021, 4, 13048−13059

sensor has shown a high level of advantages for the analysis of any drugs, due to its low cost, low analysis times, and high sensitivity with a lower detection limit.[26] The voltammetric reaction of drug molecules follows a slow kinetics mechanism; hence, the choice of modifier is mandatory for the enhanced electron-transfer rate at the electrode surface.[25] Therefore, we believe that the pyrochlore-type cubic $Sm_2Sn_2O_7$ NPs are an appropriate electrode material for the electrochemical sensing of AZN.

Herein, we have prepared the pyrochlore-type $Sm_2Sn_2O_7$ NPs using a simple coprecipitation method followed by calcination. The physicochemical properties of the material were inspected by various analytical and spectroscopic methods. After that, the prepared $Sm_2Sn_2O_7$ NPs were used as an electrode supporter or electrocatalyst for the detection of AZN in biological samples. Then the electrochemical techniques (CV and DPV) were utilized for the determination of various electrochemical parameters like detection limit, sensitivity, and selectivity to prove the efficiency of the $Sm_2Sn_2O_7$ NPs as an electrode modifier. From the tests, it was found that the $Sm_2Sn_2O_7$ NPs attained a valued sensitivity (0.27 $\mu A\ \mu M^{-1}\ cm^{-2}$) and limit of detection (4 nM) for the electrochemical sensing of AZN. The practical applicability of the designed sensor was employed for AZN detection in biological fluids and obtained good recovery results. From the outcomes, we found that the $Sm_2Sn_2O_7$ NPs are a more suitable electrocatalytic material for AZN detection, as compared to previous reports.

2. EXPERIMENTAL SECTION

2.1. Materials. Azathioprine (AZN), disodium hydrogen phosphate, sodium dihydrogen phosphate, urea, samarium nitrate hexahydrate ($Sm_2(NO_3)_3{\cdot}6H_2O$), and sodium stannate trihydrate ($Na_2SnO_3{\cdot}3H_2O$) were purchased from Sigma-Aldrich, Taiwan. These chemicals were used as received without any other pretreatment process. The phosphate buffer (0.05 M PB) electrolyte was prepared from the mixing of disodium hydrogen phosphate and sodium dihydrogen. Double-distilled (DD) water was used for the preparation of electrolytes.

2.2. Preparation of Pyrochlore $Sm_2Sn_2O_7$ by Simple Co-precipitation Method. The pyrochlore $Sm_2Sn_2O_7$ was prepared by the following procedure. First, 200 mM $Sm_2(NO_3)_3{\cdot}6H_2O$ was dispersed in 35 mL of DD water and stirred until complete ionization. Then, 35 mL of 400 mM $Na_2SnO_3{\cdot}3H_2O$ was prepared and mixed to that solution under stirring. Following that, urea (5 g) was dispersed in DD water (10 mL) and mixed with the metal-ion-containing solution. Later, the precursor mixture was kept on the stirrer for 2 h to complete the precipitation process. After the precipitation process, the supernatant liquid was decanted and the remaining precipitate was filtered using a centrifugation process. To wash out the impurities and unreacted molecules, the obtained product was washed with DD water and alcohol for 5 times. The precipitate was then dried overnight (12 h) in a hot air oven before being calcined at 1200 °C for 6 h to complete the crystallization process. Upon completion, we obtained a white powder, and the complete synthesis procedure of $Sm_2Sn_2O_7$ is illustrated in Figure 1C. Finally, the acquired white-colored material was utilized for the experimental and characterization studies.

2.3. Analytical Characterization. The crystal phase of the $Sm_2Sn_2O_7$ was analyzed by X-ray diffraction (XRD, PANalytical X'Pert PRO diffractometer) with a Cu Kα radiation source (λ = 1.541 Å). The selected diffraction (2θ) range is 15°−75°. Raman spectroscopy (Dongwoo Ramboss 500i Micro-Raman/PL spectrometer) was employed to analyze the existence of the vibrational and rotational modes of $Sm_2Sn_2O_7$. The morphology of the as-synthesized $Sm_2Sn_2O_7$ was scrutinized by field-emission scanning electron microscopy (FESEM, ZEISS Sigma 300 microscope) and high-resolution transmission electron microscopy (HRTEM; Shimadzu JEM 1200 EXSTEM). X-ray photoelectron spectroscopy analysis (XPS, Thermo Scientific MultiLab 2000) was carried out to obtain the elemental composition and oxidation states of $Sm_2Sn_2O_7$.

2.4. Electrode Fabrication and Electrochemical Measurements. For the electrode-modification process, 5 mg of $Sm_2Sn_2O_7$ NPs was weighed out and dispersed in DD water (1 mL). To get a well-dispersed catalyst solution, the dispersed solution was kept in a bath sonicator for ∼30 min at room temperature. Before the fabrication of the glassy carbon electrode (GCE, working surface; 0.07 cm^2), its surface was gently polished with alumina slurry (0.05 μm) and washed with DD water and ethanol for the removal of impurities. After that, ∼6 μL of evenly dispersed $Sm_2Sn_2O_7$ suspension was drop-coated on the mirror-like GCE surface and dried in a hot air oven maintained at 50 °C for 5 min to complete the fabrication process. Finally, the obtained $Sm_2Sn_2O_7$/GCE was utilized for further experimental studies.

Cyclic voltammetry (CV-CHI1205C) and differential pulse voltammetry (DPV-CHI900) (CH Instruments, Inc., U.S.A.) were performed to determine the electrochemical nature of AZN. The complete electrochemical experiments were conducted in a 10 mL electrolytic cell that consisted of the following standard three-electrode configuration: $Sm_2Sn_2O_7$/GCE, working electrode; platinum wire, counter electrode; and Ag/AgCl (saturated KCl), reference electrode. Before the experiments, pure nitrogen (N_2) gas was used at room temperature with a concern for the inert atmosphere.

3. RESULTS AND DISCUSSION

3.1. Crystallographic Analysis. The structural information such as crystal phase, unit cell, and composition of the prepared rare earth stannate ($Sm_2Sn_2O_7$) was examined by XRD analysis. Figure 1A displays the composition and crystallinity of the prepared product. The obtained diffraction peaks were indexed at angles of 29.41°, 34.09°, 48.98°, 58.17°, 61.03°, and 71.79°, which corresponds to the *hkl* planes of (222), (400), (440), (622), (444), and (800), respectively. All of the X-ray peaks were mainly indexed to the cubic pyrochlore-type *Fd*3*m* space group structure with a lattice constant of a = 0.09 nm (Rietveld refinement). These obtained X-ray peak positions were in good agreement and very close to those for the previously reported pyrochlore stannates followed by matches with the standard JCPDS card value (01-073-1685).[20] Moreover, this symmetry confirmed that $Sm_2Sn_2O_7$ is a long-range pyrochlore material rather than an oxygen-deficient fluorite, indicating the ordering of Sm and Sn ions on the corresponding A and B sites. Also, the presence of other impurity phases ($Sm(OH)_3$ and SnO_2) was not observed, which indicated that pure crystalline $Sm_2Sn_2O_7$ nanoparticles ($Sm_2Sn_2O_7$ NPs) were easily synthesized by following the co-precipitation process. Further, we elucidated the full-width at half-maximum (fwhm) and average particle size of prepared $Sm_2Sn_2O_7$ by the Scherrer equation (eq 1),

$$D = k\lambda/\beta\cos\theta \quad (1)$$

where D is the grain size of the particle, k is the geometry-dependent unit cell constant with a value of 0.9, λ is the wavelength (CuK, 0.15), and β is the full-width at half-maximum. The fwhm and the average particle size of the $Sm_2Sn_2O_7$ NPs were calculated to be 35 nm. Additionally, the calculated value was also compared with the selected area electron diffraction (SAED) lattice fringes values.

3.2. Raman Spectroscopy Studies. The chemical and structural "fingerprint" information as well the vibrational modes of the cubic pyrochlore $Sm_2Sn_2O_7$ NPs were obtained

https://doi.org/10.1021/acsanm.1c02591
ACS Appl. Nano Mater. 2021, 4, 13048−13059

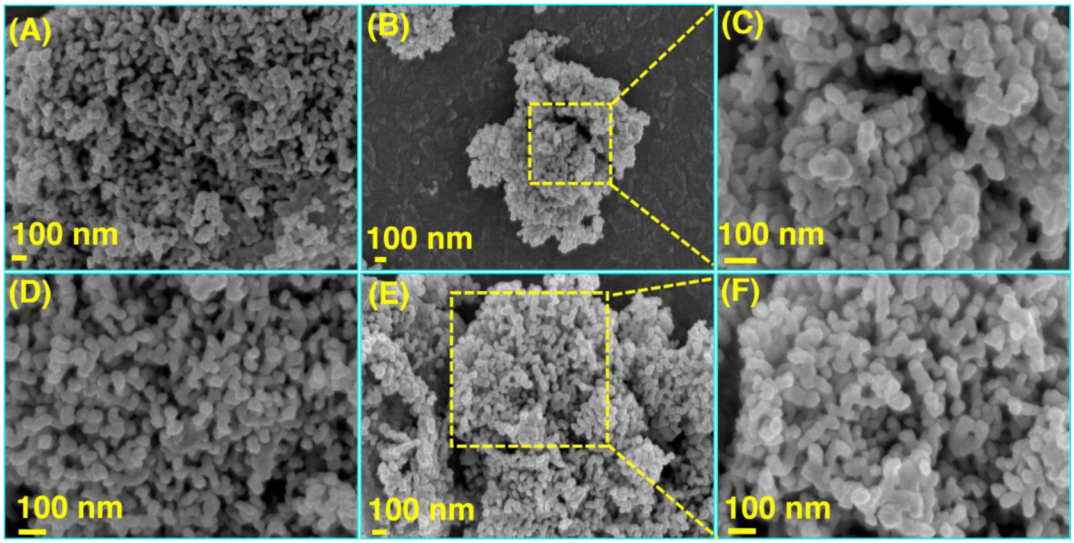

Figure 2. (A–F) Obtained FESEM images of the $Sm_2Sn_2O_7$ NPs.

by Raman spectroscopy. Figure 1B displays the Raman spectrum of the pyrochlore $Sm_2Sn_2O_7$ NPs that was completely produced by the anion substructure. On the basis of the group theory, the distorted cubic pyrochlore ($A_2B_2O_7$) structure consists of six Raman-active modes. Here, the A_{1g} mode corresponds to the vibrations of the BO_6 octahedra (mainly bending vibrations), the F_{2g} mode belongs to the mixed stretching and bending vibrations of the metal–oxygen bonds of A and B, and the E_g mode is assigned to the bending vibrations O–B–O.[20,33]

$$\text{in pyrochlore: } \Gamma_{(\text{Raman})} = A_{1g} + E_g + 4F_{2g}$$

In the unit cell, the F_{2g} mode involves the displacement of oxygen atoms on both the 8a and 48f sites, while the atomic motions associated with the E_g and A_{1g} modes are involved only in the displacement of oxygen atoms on the 48f site. It is observed that the Raman peak is obtained at ∼500 cm^{-1} because of the bending (A_{1g}) vibrations of the SnO_6 octahedra.[20,33] The F_{2g} bands for the cubic pyrochlore $Sm_2Sn_2O_7$ NPs can be visually observed at ∼343, 410, and 534 cm^{-1}, with a weak broad Raman peak located at 627 cm^{-1} due to the Sn–O bending and Sm–O bond-stretching vibrations.[20,33] Additionally, a well-defined peak mode appeared at ∼307 cm^{-1} due to the O–Sn–O bending (E_g) vibrations.[20,33] Therefore, in this present work, the acquired Raman peaks manifested the successful formation of defective and distorted $Sm_2Sn_2O_7$ NPs, and this might accelerate the feasible migration of electrons during the electrochemical reactions for the sensing of the target analyte.

3.3. Morphology and Compositional Characterization. Apart from the crystalline analysis, the surface morphology and textural factors were clearly studied by FESEM and HRTEM methods. Parts A–F of Figure 2 show the obtained FESEM images of the as-prepared cubic pyrochlore $Sm_2Sn_2O_7$ nanoparticles. It is clear from the figure that the $Sm_2Sn_2O_7$ is composed of a group of nanoparticles that are formed with an agglomeration. Also, the obtained nanoparticles are irregular in size, which is indicated in the resolution of 100 nm in range.

Further, HRTEM analysis was carried out to attain extensive morphological evidence about the $Sm_2Sn_2O_7$ NPs. Parts A–C of Figure 3 show the HRTEM images of pyrochlore-type $Sm_2Sn_2O_7$, which consists of uniform aggregate nanoparticles with a diameter of 100–200 nm in the range. More details can be deduced from parts B and C of Figure 3, which indicate that each aggregate consists of a large number of randomly sized nanoparticles with a size of 10 nm. Then the typical lattice-resolved HRTEM images of the $Sm_2Sn_2O_7$ NPs indicate the formation of surface-defect-rich, crystal-clear lattice fringes with interplanar distances of 0.30 and 0.18 nm, which match well with the (220) and (440) *hkl* XRD planes of cubic $Sm_2Sn_2O_7$, respectively. Also, the bright selected area electron diffraction (SAED) patterns of the $Sm_2Sn_2O_7$ NPs (Figure 3D) were indexed to the diffraction from the plane values of the (622), (222), and (440) $Sm_2Sn_2O_7$ NPs, designating that the nanoparticles have polycrystalline properties. Finally, the existence of the elements and their corresponding compositions was confirmed by energy-dispersive spectroscopy (EDS) mapping analysis, and the acquired elemental mapping images are presented in Figure 3E–I. Parts G–I of Figure 3 represent that elements like samarium (Sm), tin (Sn), and oxygen (O) are regularly present in the synthesized $Sm_2Sn_2O_7$ NPs without any other elements. These surface analysis results proved that the pyrochlore-type $Sm_2Sn_2O_7$ NPs are present in the form of pure nanoparticles without any phase change, and the pure, smooth surface nanoparticles enhance the electrochemical activity.[34]

3.4. XPS Analysis. The accurate oxidation state and surface chemical composition information of $Sm_2Sn_2O_7$ were investigated by XPS analysis, and the obtained results are portrayed in Figure 4A–D. Figure 4A displays the overall survey spectrum of the $Sm_2Sn_2O_7$ NPs. Figure 4B indicates the Sm 3d spectrum, which is deconvoluted to the broad characteristic peaks at 1111.2 and 1084.7 eV corresponding to the subshells of Sm $3d_{3/2}$ and Sm $3d_{5/2}$, respectively (oxidation states Sm^{3+} and Sm^{2+}).[35] The low-intensity band of Sm^{2+} indicates the presence of oxygen vacancies. Figure 4C shows that the peaks at 496.8 and 488.4 eV indicate the presence of Sn 3d subshells corresponding to the oxidation states of Sn $3d_{3/2}$ and Sn $3d_{5/2}$, respectively.[25,35] Also, the fitting O 1s (Figure 4D) spectra give two bands: the peak obtained at 532.2 eV for the surface lattice oxygen (O_{latt}), and the band at 534 eV due to the loosely bound surface oxygen (O_{ads}).[20,35] These two different oxygen species determine the relative contents of the oxygen

https://doi.org/10.1021/acsanm.1c02591
ACS Appl. Nano Mater. 2021, 4, 13048–13059

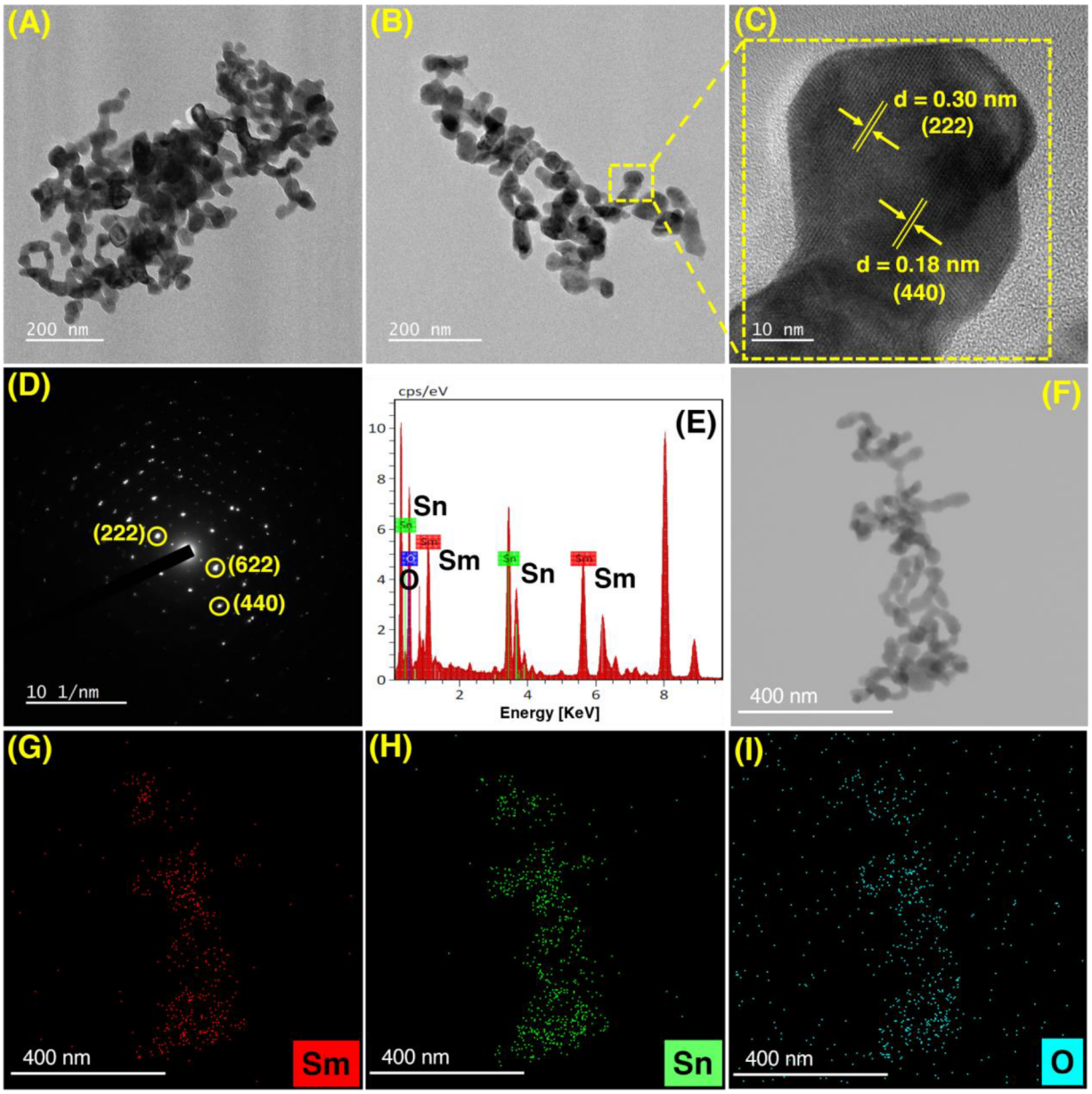

Figure 3. (A, B) HRTEM images of the $Sm_2Sn_2O_7$ NPs. (C, D) HRTEM lattice fringes and SAED patterns of the $Sm_2Sn_2O_7$ NPs. (E) EDS spectrum. (F) HRTEM electron image. (G–I) Mapping images of the $Sm_2Sn_2O_7$ NPs.

vacancies. Therefore, the obtained results give a detailed report about the formation of the $Sm_2Sn_2O_7$ NPs and match well with previously reported results. Moreover, the existence of oxygen vacancies can easily impart the migration of bulky oxygen ions, which leads to a faster electrocatalytic reaction.

3.5. Electrochemical Impedance Spectroscopy of the $Sm_2Sn_2O_7$/GCE. The electrochemical natures of the bare GCE and $Sm_2Sn_2O_7$/GCE were evaluated by the electrochemical impedance spectroscopy (EIS) technique in 0.1 M KCl with 5 mM $Fe[(CN)_6]^{3-/4-}$, and the results are portrayed in Figure S1 (frequency = 100 kHz to 100 mHz, applied potential = 0.43 V). The bare GCE and $Sm_2Sn_2O_7$/GCE show a semicircle that depicts the electron-transfer resistance, and the obtained linear part characterizes the diffusion-limited process. From Figure S1, the R_{ct} values of the bare GCE and $Sm_2Sn_2O_7$/GCE were calculated to be 364 Ω and 681 Ω, respectively. Compared to the bare GCE, the $Sm_2Sn_2O_7$/GCE shows higher R_{ct} values, which is due to the electrostatic repulsion between the $Fe[(CN)_6]^{3-/4-}$ system and the negatively charged pyrochlore metal oxide.[23] This results confirms that the $Sm_2Sn_2O_7$ nanoparticles were well-established on the GCE surface.

3.6. Electrochemical Evaluation of AZN at the $Sm_2Sn_2O_7$/GCE. The electrocatalytic activity of the $Sm_2Sn_2O_7$/GCE against AZN was measured by the CV technique over the potential window between 0.6 and −1.0 V. Figure 5A exhibits the CV signals of the 100 μM AZN in 0.05 M PB solution for the (a) bare GCE and (b) $Sm_2Sn_2O_7$/GCE at a 50 mV/s sweep rate. At the bare GCE, AZN was electrochemically reduced at −0.56 V and showed a current response of −4.63 μA. In the meantime, the $Sm_2Sn_2O_7$/GCE showed an enriched peak current of −8.55 μA at a potential of −0.55 V. From Figure 5B, it can be seen that the $Sm_2Sn_2O_7$/GCE provided a 1.8-fold greater current response than the bare GCE. The bare GCE and $Sm_2Sn_2O_7$/GCE show one cathodic peak in the forward scan and one anodic peak during

https://doi.org/10.1021/acsanm.1c02591
ACS Appl. Nano Mater. 2021, 4, 13048−13059

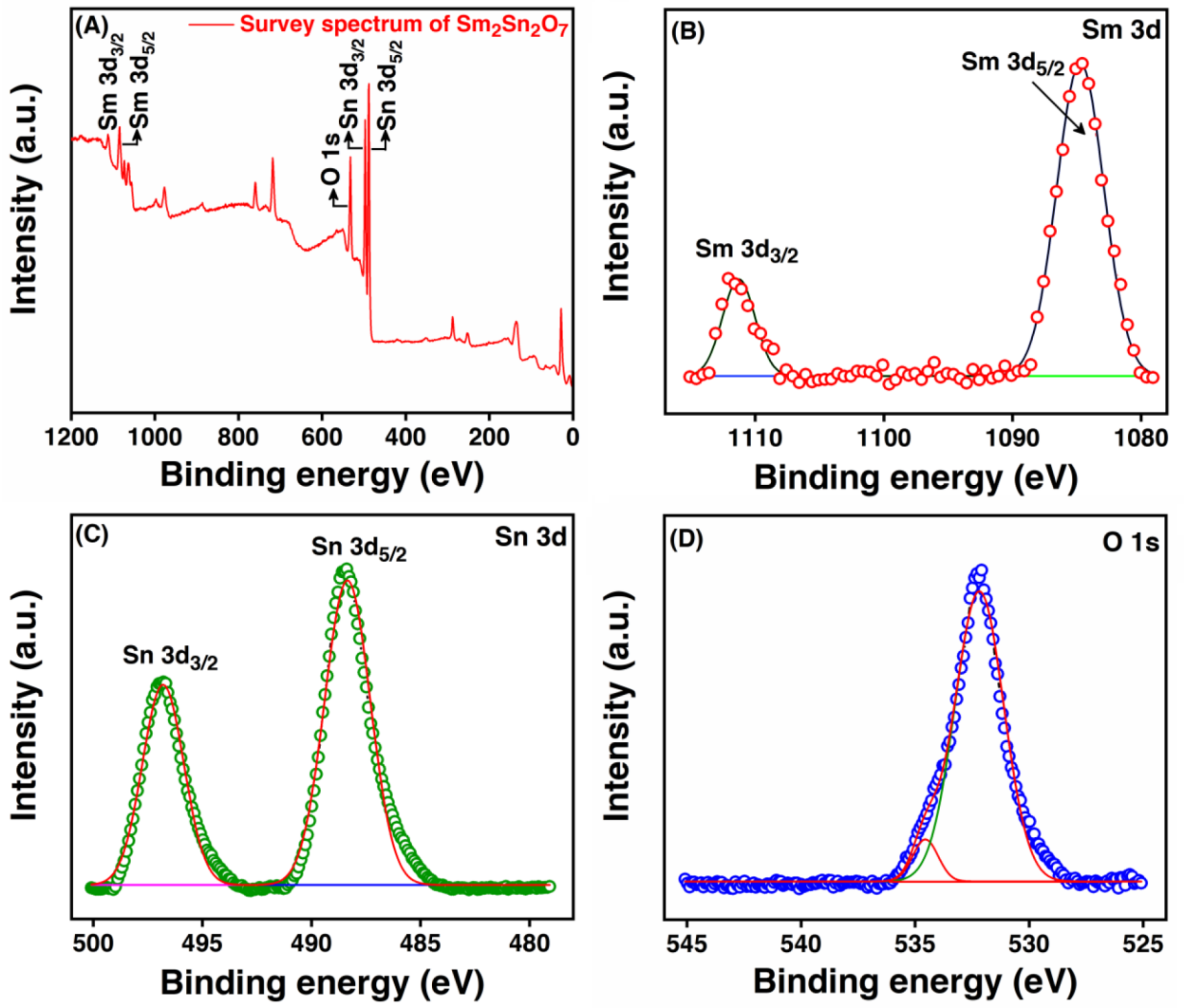

Figure 4. (A) Survey spectrum. Highly magnified XPS spectroscopy: (B) Sm 3d, (C) Sn 3d, and (D) O 1s.

the reverse scan. The cathodic peak showed electrochemical reduction of the nitro group ($-NO_2$) that was present in the AZN into the related hydroxylamine ($-NHOH$) with the involvement of an identical number of electrons ($4e^-$) and protons ($4H^+$).[26,35] On moving toward the positive scan, a small anodic peak was obtained owing to the transformation of hydroxylamine to the nitroso ($-N{=}O$) group. The extensive electrochemical conversion of AZN at the $Sm_2Sn_2O_7$-modified GCE is shown in Scheme 1.

Additionally, the concentration effect of AZN on the $Sm_2Sn_2O_7$/GCE was analyzed at a sweep rate of 50 mV/s. For this study, AZN was gradually added from 50 to 300 μM, and the related CVs are portrayed in Figure 5C. From Figure 5C, it can be seen that the cathodic peak current of AZ was steadily enhanced with the increasing concentration of AZN. Moreover, a fine linear relationship was noticed between the AZN peak current versus the concentration of AZN. The corresponding linear plot and the linear correlation equation of $y = -0.059x - 2.698$ ($R^2 = 0.975$) are shown in Figure 5D. The $Sm_2Sn_2O_7$-modified GCE showed significant electrochemical sensing behavior for the AZN reduction.

3.7. pH Optimization. Due to the impact of the electrolyte's pH on the peak current and the peak potential of the CV curves, optimizing a suitable pH is an essential parameter for electrocatalytic applications. To analyze the pH effect, CV was performed with AZN (100 μM) in PB solution (0.05 M) at various pH values from 5.0 to 11.0 over the $Sm_2Sn_2O_7$/GCE. As seen in Figure 6A, the cathodic peak current was raised from pH 5.0 to 7.0. The peak current then was lowered upon increasing the pH from 7.0 to 11.0. Interestingly, the peak potential of AZN was moved to a negative potential upon increasing the pH from 5.0 to 11.0. This is due to the presence of more H^+ ions in low pH and OH^- ions in higher pH which may influence the electrochemical activity of AZN at the $Sm_2Sn_2O_7$/GCE. Owing to the existence of the same number of electrons and protons in the neutral medium, a higher reduction current was found in pH 7.0 (Figure 6B). As a result, pH 7.0 was chosen as the favored electrolyte for the following electrochemical investigations.

3.8. Sweep-Rate Studies. To investigate the impact of scan rate for the AZN reduction, CV was employed on the $Sm_2Sn_2O_7$/GCE at different scan rates. Figure 6C presents the CVs of 100 μM AZN at ramping scan rates from 20 to 200 mV/s. From Figure 6C, when the sweep rate was ramped from lower to higher values (20 to 200 mV/s), the peak current of AZN was linearly raised. Moreover, the reduction peak

https://doi.org/10.1021/acsanm.1c02591
ACS Appl. Nano Mater. 2021, 4, 13048−13059

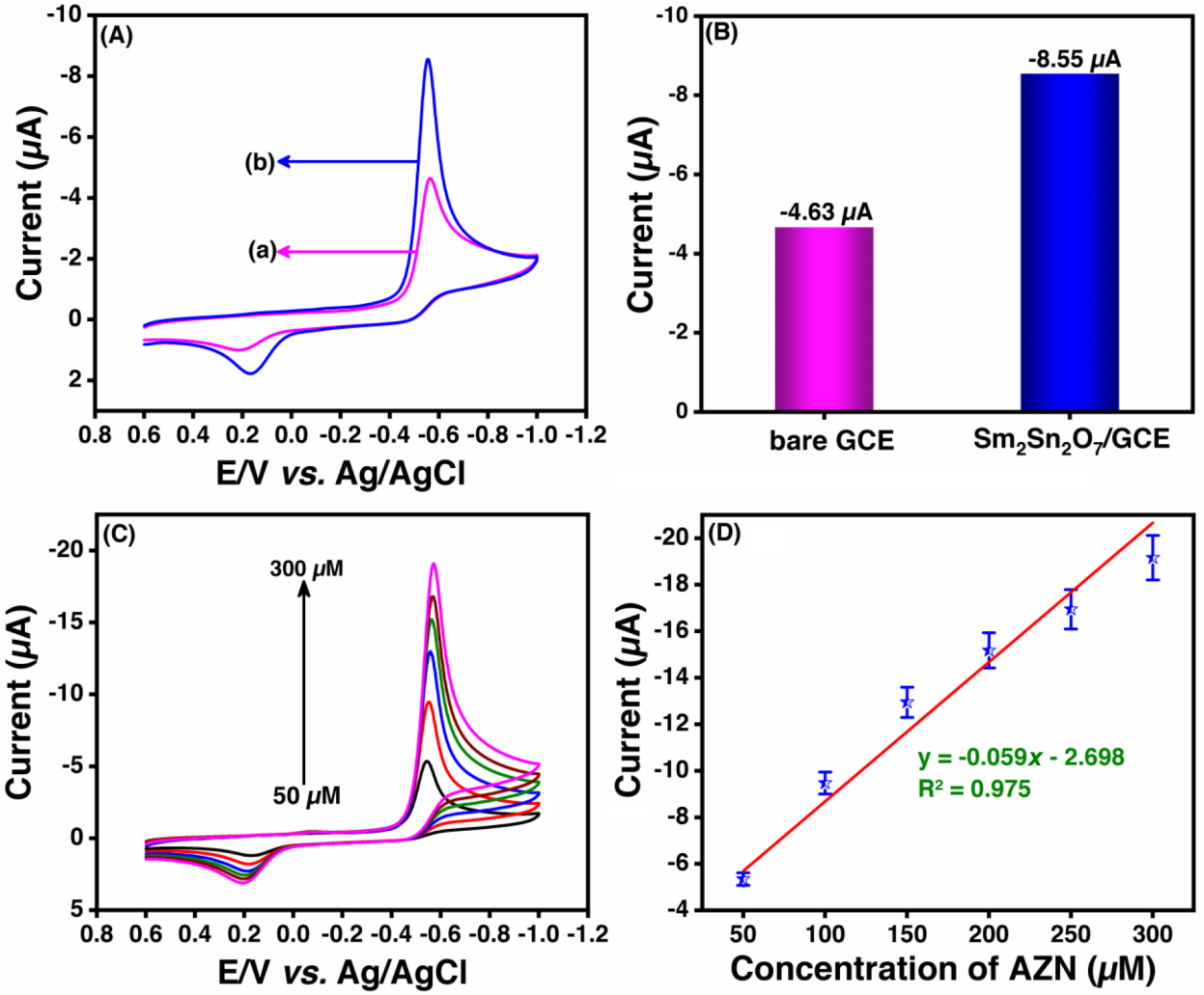

Figure 5. (A) CVs of the (a) bare GCE and (b) $Sm_2Sn_2O_7$/GCE with the presence of 100 μM AZN. (B) Corresponding bar diagram; cathodic current response of 100 μM AZN at the bare GCE and $Sm_2Sn_2O_7$/GCE. (C) CVs of various concentrations of AZN (50−300 μM) on the $Sm_2Sn_2O_7$/GCE. (D) Calibration plot: concentration of AZN vs cathodic current. All of these experiments were performed in 0.05 M PB solution (pH 7.0) at 50 mV/s.

Scheme 1. Electrocatalytic Reduction Mechanism of AZN at the $Sm_2Sn_2O_7$ Modified GCE

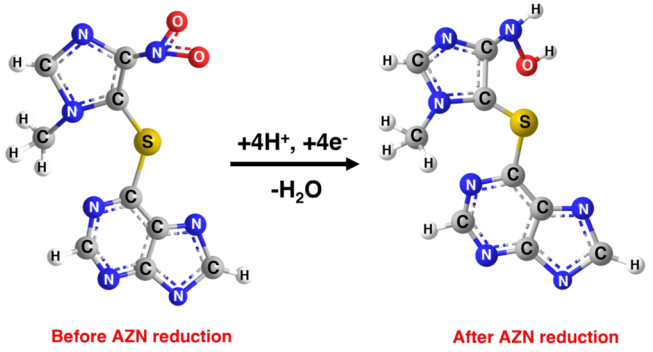

potential was also negatively shifted when increasing the scan rate from lower to higher. In addition to that, a good linear relationship was achieved for the peak current versus square root of the scan rate (I_{pc} vs $v^{1/2}$) with a linear regression equation of $y = -1.276x - 1.814$ with a correlation coefficient of $R^2 = 0.995$ (Figure 6D). This discussion implies that the electrochemical reduction of AZN at the $Sm_2Sn_2O_7$/GCE is a diffusion-controlled process rather than an adsorption-controlled one.

3.9. Determination of AZN. To evaluate the linear range, limit of detection (LOD), and sensitivity of the $Sm_2Sn_2O_7$/GCE for AZN determination, DPV was executed with the gradual addition of AZN in 0.05 M PB (pH 7.0) solution. Figure 7A shows the DPV responses at the $Sm_2Sn_2O_7$/GCE with concentrations of AZN from 0.01 to 948 μM in the potential window between 0 and −1.0 V. It can be observed that, when moving from lower to higher concentration, the reduction peak current of AZN was linearly increased with the peak shift toward the negative direction. Interestingly, a fine linear relationship was obtained between the concentration of AZN and the reduction peak current, and the related linear plot is displayed in Figure 7B with a correlation equation of $y = -0.019x - 0.654$ ($R^2 = 0.991$). The obtained lower-concentration DPV signals of AZN and its corresponding linear calibration plot are displayed in parts C and D of Figure 7, respectively. Moreover, the limit of detection was calculated by using the IUPAC convention of

$$\mathrm{LOD} = 3N/S \quad (2)$$

https://doi.org/10.1021/acsanm.1c02591
ACS Appl. Nano Mater. 2021, 4, 13048−13059

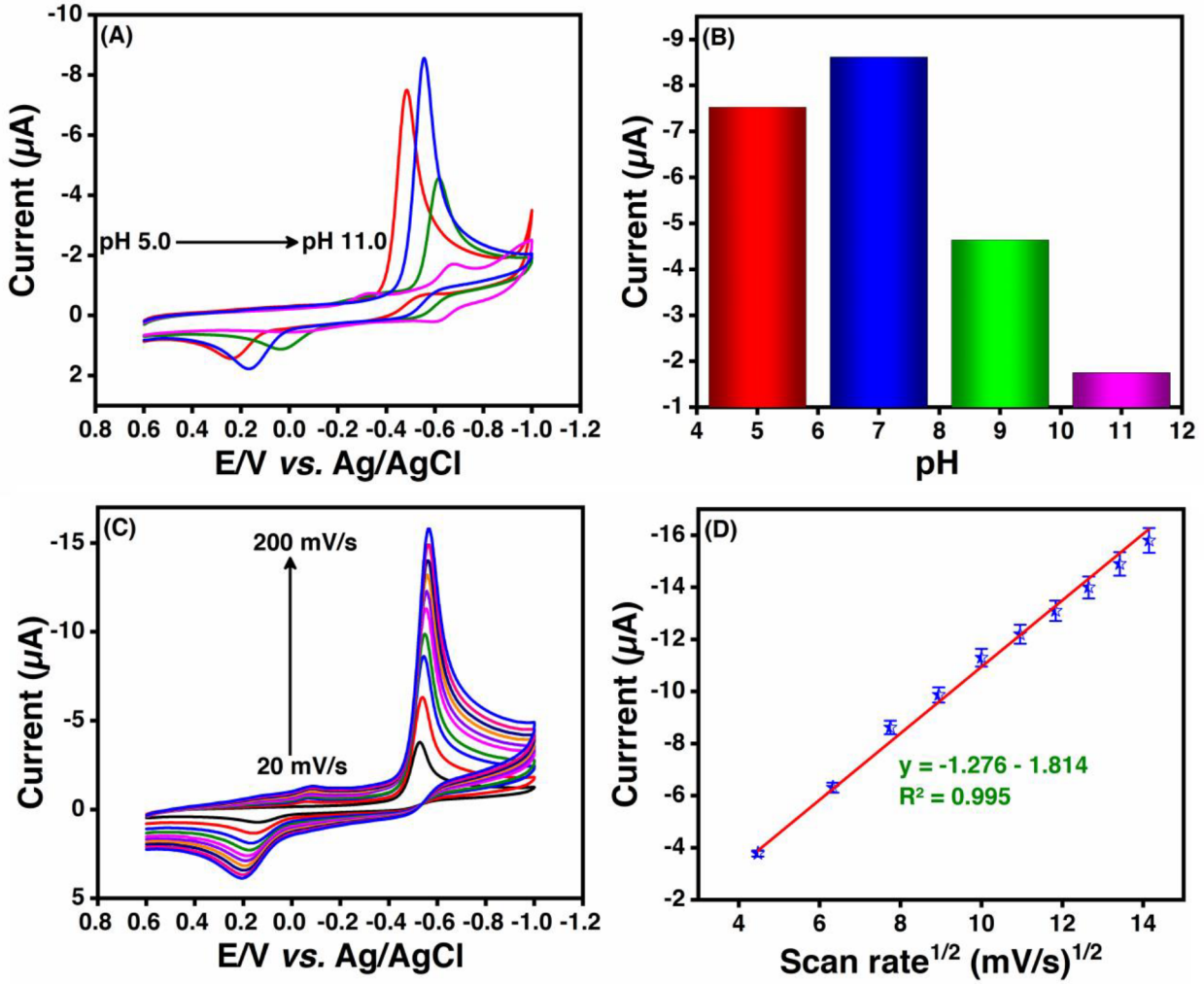

Figure 6. (A) CV histograms of the $Sm_2Sn_2O_7$/GCE at different pH ranges such as 5.0, 7.0, 9.0, and 11.0 with 100 μM AZN. (B) Bar diagram: pH vs cathodic peak current of AZN. (C) CVs on the $Sm_2Sn_2O_7$/GCE for 100 μM AZN over different sweeping rates (20−200 mV/s). (D) Calibration plot: different sweep rates vs cathodic current of AZN.

In eq 2, N is the standard deviation of three blank DPV signals, and S is the value of the slope obtained from the linear plot of DPV. The LOD was calculated to be 4 nM. Additionally, the sensitivity of the constructed sensor was calculated to be 0.27 μA μM^{-1} cm^{-2}. Furthermore, the obtained analytical credentials such as LOD, sensitivity, and wide linear ranges (0.01−948 μM) of the $Sm_2Sn_2O_7$/GCE for AZN determination were correlated with the previous studies of AZN determination and are listed in Table 1. From the list in the table, it is clear that the $Sm_2Sn_2O_7$/GCE showed very improved and comparable analytical credential results for the determination of AZN. These results suggest that the $Sm_2Sn_2O_7$/GCE is an impressive electrochemical sensor for the determination of AZN.

3.10. Selectivity, Repeatability, Reproducibility, and Stability Studies. Selectivity is an essential characterization for a newly developed electrochemical sensor. The interference studies for the $Sm_2Sn_2O_7$/GCE for AZN detection were conducted by the DPV technique with the addition of potentially interfering compounds in 0.05 M PB solution (pH 7.0) containing 100 μM AZN under N_2 gas atmosphere. Figure 8A shows the DPV curves of 100 μM ascorbic acid (AA), catechol (CC), dopamine (DOP), glucose (GLU), uric acid (UA), Ca^{2+}, Fe^{2+}, Mg^{2+}, Ni^{2+}, Zn^{2+}, nitrobenzene (NB), and nifedipine (NFP) in the presence of 100 μM AZN. As can be seen from the acquired DPV findings, with the presence of interfering compounds like biomolecules, metal ions, and nitro group-containing drugs, an insignificant decrease in the peak current and a slight shift in the peak potential of AZN reduction were observed with an RSD of less than ±5% in peak current value. These findings show that the $Sm_2Sn_2O_7$/GCE has excellent selectivity for the determination of AZN.

Moreover, the repeatability of the as-constructed $Sm_2Sn_2O_7$/GCE sensor was analyzed by 10 continuous DPV measurements for 100 μM AZN, and the corresponding DPV results are shown in Figure 8B. The RSD value for the repeatability study was found to be 3%. In addition to that, five individual GCEs were drop-coated with $Sm_2Sn_2O_7$ and utilized for the reproducibility studies for AZN. Figure 8C shows the DPV curves for 100 μM AZN in 0.05 M PB solution for five different GCEs coated with $Sm_2Sn_2O_7$. As a result, acceptable RSD values for AZN determination were achieved, with an RSD of ∼5%. Additionally, the storage stability of the constructed sensor was tested after storage for 15 days, and the DPV results are displayed in Figure 8D. The retained responses were >90%, which indicates the good storage

https://doi.org/10.1021/acsanm.1c02591
ACS Appl. Nano Mater. 2021, 4, 13048−13059

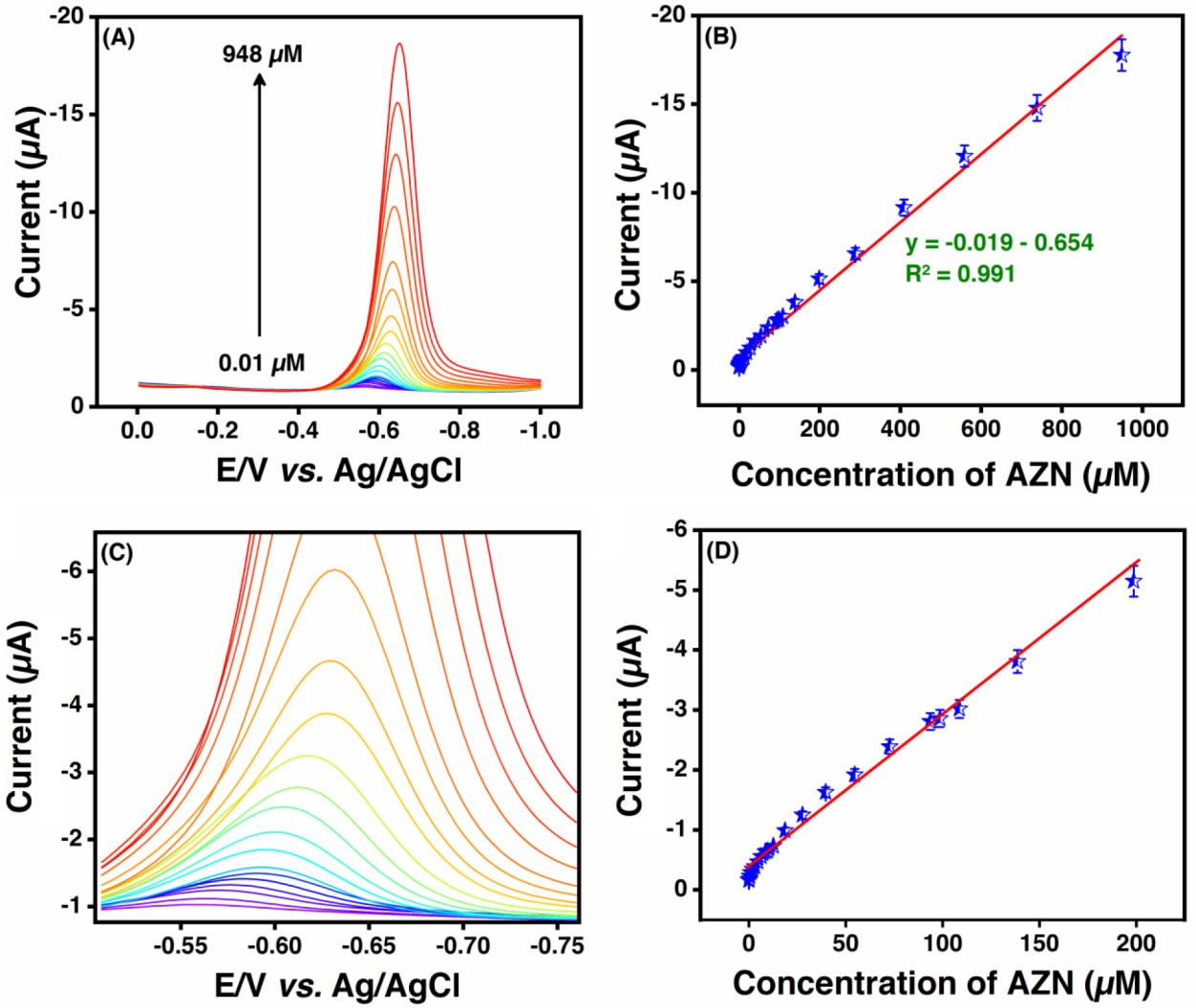

Figure 7. (A) DPVs for the $Sm_2Sn_2O_7$/GCE with the gradual addition of AZN (0.01 to 948 μM) in 0.05 M PB solution. (B) Calibration plot: concentration of AZN vs DPV currents. (C, D) Lower-concentration DPV signals of AZN and its linear calibration plot between the concentration of AZN and the DPV current response corresponding to those in (A) and (B).

Table 1. Comparison: Determination of AZN at the $Sm_2Sn_2O_7$/GCE Compared with Previously Reported AZN Sensors

technique	electrodes	LOD (nM)	linear range (μM)	ref
CV	CNP/N/GCE	80	0.2−2.0	36
CV	NDG/CS/GCE	65	0.2−100	25
CV	Ag NPs @ graphene-modified CPE	68	0.7−100	26
DPV	Au NNs	33	0.5−2300	37
DPV	$Sm_2Sn_2O_7$/GCE	4	0.01−948	this work

stability of the $Sm_2Sn_2O_7$/GCE for AZN determination. In conclusion, the attained electrochemical results revealed that the constructed $Sm_2Sn_2O_7$/GCE had excellent selectivity and satisfactory repeatability, reproducibility, and storage stability.

3.11. Practical Analysis. To demonstrate the practical application of the $Sm_2Sn_2O_7$/GCE, the electrochemical detection of AZN was evaluated in human urine and blood serum samples that were acquired from Chang Gung University following the Committee's laws and regulations, and the experimental procedure was followed. Both samples (5 mL) were diluted 10 times with PB (pH 7.0, 0.05 M) solution and centrifuged at 6000 rpm for 20 min. The clear solution was collected and utilized in the DPV experiments. In both cases, DPV was executed in PB solution (0.05 M, pH 7.0) under the optimal conditions. The DPV current response was recorded with the inclusion of the acquired sample. In the blank solution, there is no current response. After that, different concentrations of AZN were spiked gradually, and the obtained DPV curves are shown in Figure S2A and B. From Figure S2A and B, it can be observed that the reduction peak current was linearly increased with the increasing concentration of AZN. The recovery results of AZN in both real samples were calculated using the standard addition method, and the obtained credentials are listed in Table S1. Table S1 shows the satisfactory recovery results of 98−99.20% (blood serum) and 97.16−98.87% (urine sample). In conclusion, the developed $Sm_2Sn_2O_7$/GCE sensor exhibits satisfactory recovery results for the real-time analysis of AZN in human blood serum and urine samples. The as-prepared cubic pyrochlore $Sm_2Sn_2O_7$ NPs proved their practical application in biological

https://doi.org/10.1021/acsanm.1c02591
ACS Appl. Nano Mater. 2021, 4, 13048−13059

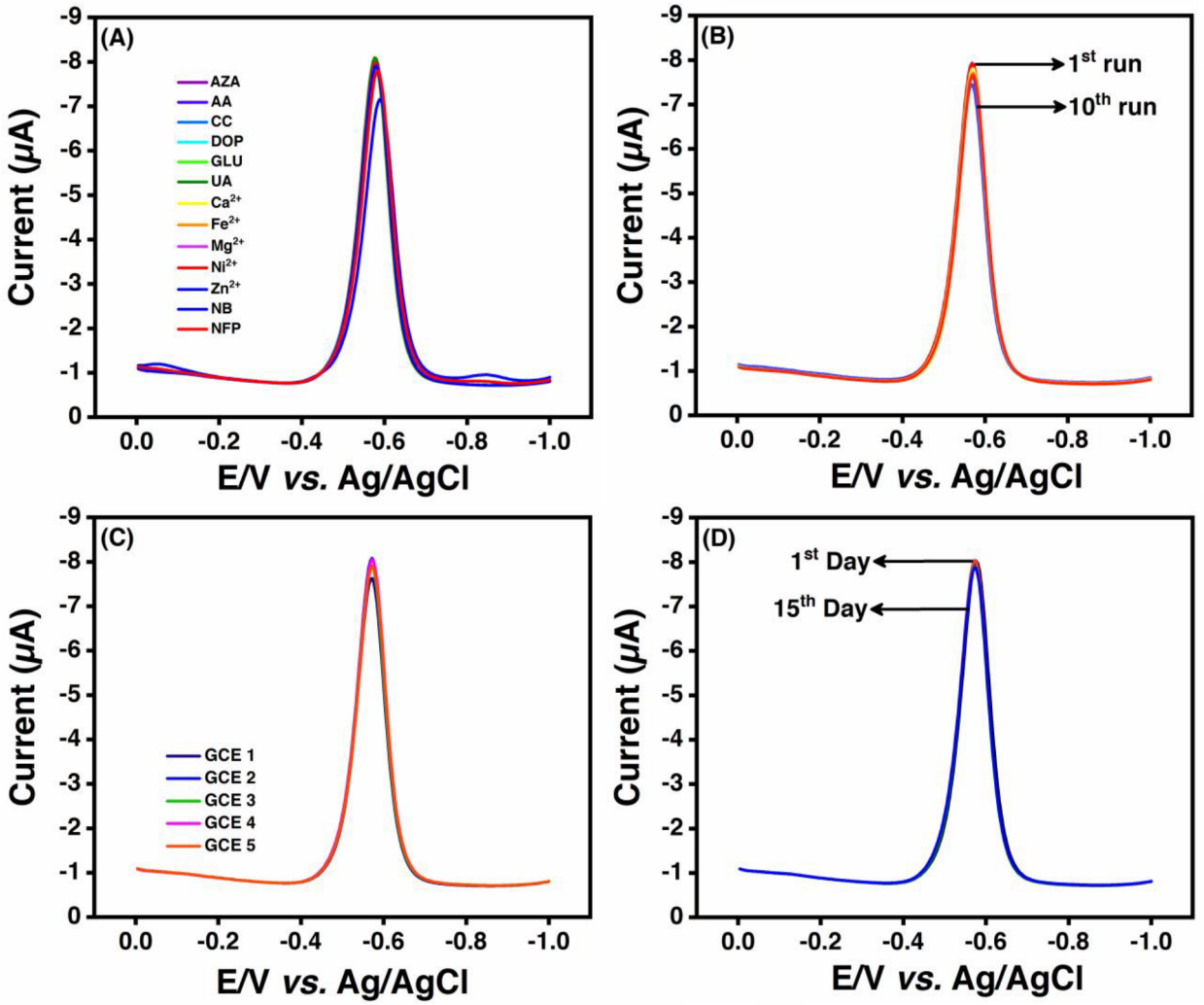

Figure 8. (A) DPV curves of 100 μM AZN with the presence of interferences such as ascorbic acid (AA), catechol (CC), dopamine (DOP), glucose (GLU), uric acid (UA), Ca^{2+}, Fe^{2+}, Mg^{2+}, Ni^{2+}, Zn^{2+}, nitrobenzene (NB), and nifedipine (NFP) in 0.05 M PB solution (pH 7.0). (B) DPV curves of 10 consecutive measurements for 100 μM AZN. (C) DPV curves for 100 μM AZN at five different GCEs coated with the $Sm_2Sn_2O_7$/GCE. (D) DPV curves of storage stability studies. The entire DPV experiment was carried out in a 0.05 M PB (pH 7.0) solution.

molecules and structurally related pharmaceutical drugs for the sensing of AZN.

4. CONCLUSION

A simple co-precipitation method was used for the synthesis of cubic pyrochlore $Sm_2Sn_2O_7$ NPs. The as-synthesized $Sm_2Sn_2O_7$ was characterized by using different physiochemical characterization methods such as XRD, Raman spectroscopy, and XPS. The morphological observations were carried out using FESEM and HRTEM techniques. After that, the cubic pyrochlore $Sm_2Sn_2O_7$ NPs were employed as an electrode material with the aid of a glassy carbon electrode, and the fabricated $Sm_2Sn_2O_7$/GCE was used for the electrochemical determination of AZN. It was demonstrated that the proposed electrode delivered excellent electrocatalytic activity for AZN detection with an LOD of 4 nM and a sensitivity of 0.27 μA μM^{-1} cm^{-2} due to the distorted cubic pyrochlore with defective oxygen vacancies, which might accelerate the electron mobility during the electrochemical reactions. Along with that, the $Sm_2Sn_2O_7$/GCE retains superior selectiveness with the coexistence of related nitro groups containing drugs, biological molecules, and metal ions. The practical applicability of the AZN sensor was tested in the human blood serum and urine samples, and the $Sm_2Sn_2O_7$ NPs revealed acceptable recovery results for the potential biological applications. From the obtained electrochemical findings, we believe that the as-prepared $Sm_2Sn_2O_7$ should be a promising candidate for the electrochemical determination of AZN in clinical and biological applications.

■ ASSOCIATED CONTENT

Supporting Information

The Supporting Information is available free of charge at https://pubs.acs.org/doi/10.1021/acsanm.1c02591.

EIS spectra (bare GCE and $Sm_2Sn_2O_7$/GCE), tabulation for the real sample analysis of AZN in biological samples, and DPV results for real sample analysis (PDF)

■ AUTHOR INFORMATION

Corresponding Author

Shen-Ming Chen − *Electroanalysis and Bioelectrochemistry Lab, Department of Chemical Engineering and Biotechnology, National Taipei University of Technology, Taipei 106*

https://doi.org/10.1021/acsanm.1c02591
ACS Appl. Nano Mater. 2021, 4, 13048−13059

Taiwan, ROC; orcid.org/0000-0002-0132-9161; Phone: +886-2270-17147; Email: smchen78@ms15.hinet.net; Fax: +886-2270-25238

Authors

Ramachandran Rajakumaran − *Electroanalysis and Bioelectrochemistry Lab, Department of Chemical Engineering and Biotechnology, National Taipei University of Technology, Taipei 106 Taiwan, ROC*

Karuppaiah Balamurugan − *Electroanalysis and Bioelectrochemistry Lab, Department of Chemical Engineering and Biotechnology, National Taipei University of Technology, Taipei 106 Taiwan, ROC*

Ramaraj Sukanya − *Electroanalysis and Bioelectrochemistry Lab, Department of Chemical Engineering and Biotechnology, National Taipei University of Technology, Taipei 106 Taiwan, ROC;* orcid.org/0000-0002-9033-4201

Carmel B. Breslin − *Department of Chemistry, Maynooth University, W23F2H6 Maynooth, Co. Kildare, Ireland;* orcid.org/0000-0002-0586-5375

Complete contact information is available at: https://pubs.acs.org/10.1021/acsanm.1c02591

Notes

The authors declare no competing financial interest.

■ ACKNOWLEDGMENTS

The authors acknowledge the Ministry of Science and Technology (MOST 110-2113-M-027-003), Taiwan.

■ REFERENCES

(1) Öztürk, E.; Sarılmaz, E. The Investigation of the Photoluminescent and Piezoelectric Effect of Eu^{3+} Doped $Y_2Ti_2O_7$ and $Sm_2Ti_2O_7$ Host Crystals. *Mater. Chem. Phys.* **2020**, *239*, 122085.

(2) Garbout, A.; Turki, T.; Férid, M. Structural and Photoluminescence Characteristics of Sm^{3+} Activated $RE_2Ti_2O_7$ (RE = Gd, La) as Orange-Red Emitting Phosphors. *J. Lumin.* **2018**, *196*, 326−336.

(3) Zhang, P.; Wang, W.; Liu, J.; Zhou, C.; Zhou, J. J.; Xu, L.; Chen, L. N-Doped Carbon-Wrapped Cobalt-Manganese Oxide Nanosheets Loaded into a Three-Dimensional Graphene Nanonetwork as a Free-Standing Anode for Lithium-Ion Storage. *ACS Appl. Nano Mater.* **2021**, *4* (4), 3619−3630.

(4) Karthik, R.; Vinoth Kumar, J.; Chen, S. M.; Seerangan, K.; Karuppiah, C.; Chen, T. W.; Muthuraj, V. Investigation on the Electrocatalytic Determination and Photocatalytic Degradation of Neurotoxicity Drug Clioquinol by $Sn(MoO_4)_2$ Nanoplates. *ACS Appl. Mater. Interfaces* **2017**, *9* (31), 26582−26592.

(5) Zhang, S.; Wang, K.; Zhang, X.; Feng, P.; Li, F. α-$AgVO_3$ Nanowire/Graphene Oxide Composite Paper Electrodes for Lithium-Ion Batteries. *ACS Appl. Nano Mater.* **2021**, *4* (3), 2452−2461.

(6) Abinaya, M.; Rajakumaran, R.; Chen, S. M.; Karthik, R.; Muthuraj, V. In Situ Synthesis, Characterization, and Catalytic Performance of Polypyrrole Polymer-Incorporated Ag_2MoO_4 Nanocomposite for Detection and Degradation of Environmental Pollutants and Pharmaceutical Drugs. *ACS Appl. Mater. Interfaces* **2019**, *11* (41), 38321−38335.

(7) Chanda, K.; Maiti, S.; Sarkar, S.; Bairi, P.; Thakur, S.; Sardar, K.; Besra, N.; Das, N. S.; Chattopadhyay, K. K. Hierarchical Assembly of MnO_2Nanosheet on $CuCo_2O_4$ Nanoflake over Fabric Scaffold for Symmetric Supercapacitor. *ACS Appl. Nano Mater.* **2021**, *4* (2), 1420−1433.

(8) Wang, Z.; Zhu, H.; Ai, L.; Liu, X.; Lv, M.; Wang, L.; Ma, Z.; Zhang, Z. Catalytic Combustion of Soot Particulates over Rare-Earth Substituted $Ln_2Sn_2O_7$ Pyrochlores (Ln = La, Nd and Sm). *J. Colloid Interface Sci.* **2016**, *478*, 209−216.

(9) Marlton, F. P.; Zhang, Z.; Zhang, Y.; Proffen, T. E.; Ling, C. D.; Kennedy, B. J. Lattice Disorder and Oxygen Migration Pathways in Pyrochlore and Defect-Fluorite Oxides. *Chem. Mater.* **2021**, *33* (4), 1407−1415.

(10) Liu, Q.; Xu, M.; Low, Z. X.; Zhang, W.; Tao, F.; Liu, F.; Liu, N. Controlled Synthesis of Pyrochlore $Pr_2Sn_2O_7$ Nanospheres with Enhanced Gas Sensing Performance. *RSC Adv.* **2016**, *6* (26), 21564−21570.

(11) Matsumoto, U.; Ogawa, T.; Kitaoka, S.; Moriwake, H.; Tanaka, I. First-Principles Study on the Stability of Weberite-Type, Pyrochlore, and Defect-Fluorite Structures of $A_2^{3+}B_2^{4+}O_7$(A = Lu^{3+}-La^{3+}, B = Zr^{4+}, Hf^{4+}, Sn^{4+}, and Ti^{4+}). *J. Phys. Chem. C* **2020**, *124* (37), 20555−20562.

(12) Lebedev, D.; Povia, M.; Waltar, K.; Abdala, P. M.; Castelli, I. E.; Fabbri, E.; Blanco, M. V.; Fedorov, A.; Copéret, C.; Marzari, N.; et al. Highly Active and Stable Iridium Pyrochlores for Oxygen Evolution Reaction. *Chem. Mater.* **2017**, *29* (12), 5182−5191.

(13) Park, J.; Risch, M.; Nam, G.; Park, M.; Shin, T. J.; Park, S.; Kim, M. G.; Shao-Horn, Y.; Cho, J. Single Crystalline Pyrochlore Nanoparticles with Metallic Conduction as Efficient Bi-Functional Oxygen Electrocatalysts for Zn-Air Batteries. *Energy Environ. Sci.* **2017**, *10* (1), 129−136.

(14) Feng, Q.; Zhang, Z.; Huang, H.; Yao, K.; Fan, J.; Zeng, L.; Williams, M. C.; Li, H.; Wang, H. An Effective Strategy to Tune the Oxygen Vacancy of Pyrochlore Oxides for Electrochemical Energy Storage and Conversion Systems. *Chem. Eng. J.* **2020**, *395*, 124428.

(15) Kaliyaperumal, C.; Jayabalan, S.; Sankarakumar, A.; Paramasivam, T. Structural and Electrical Characteristics of Nanocrystalline $La_2Sn_2O_7$ Pyrochlore. *Solid State Sci.* **2020**, *105*, 106245.

(16) Zinatloo-Ajabshir, S.; Morassaei, M. S.; Amiri, O.; Salavati-Niasari, M. Green Synthesis of Dysprosium Stannate Nanoparticles Using Ficus Carica Extract as Photocatalyst for the Degradation of Organic Pollutants under Visible Irradiation. *Ceram. Int.* **2020**, *46* (5), 6095−6107.

(17) Rajakumaran, R.; Sukanya, R.; Chen, S. M.; Karthik, R.; Breslin, C. B.; Shafi, P. M. Synthesis and Characterization of Pyrochlore-Type Praseodymium Stannate Nanoparticles: An Effective Electrocatalyst for Detection of Nitrofurazone Drug in Biological Samples. *Inorg. Chem.* **2021**, *60* (4), 2464−2476.

(18) Prabhakaran, D.; Wang, S.; Boothroyd, A. T. Crystal Growth of Pyrochlore Rare-Earth Stannates. *J. Cryst. Growth* **2017**, *468*, 335−339.

(19) Abraham, A.; Gupta, S. K.; Mohan, S.; Abdou, H.; Mao, Y. Defect-Induced Optical and Electrochemical Properties of $Pr_2Sn_2O_7$ Nanoparticles Enhanced by Bi^{3+} Doping. *J. Mater. Res.* **2020**, *35* (9), 1214−1224.

(20) Duan, P.; Han, C.; Zheng, Y.; Cai, G.; Zhong, F.; Xiao, Y. $A_2B_2O_7$ (A = La, Pr, Nd, Sm, Gd and B = Ti, Zr, Sn) Ceramics for Mild-Temperature NO_2 Sensing and Reduction. *J. Alloys Compd.* **2020**, *831* (2), 154866.

(21) Karabulut, Y.; Ayvacikli, M.; Canimoglu, A.; Guinea, J. G.; Kotan, Z.; Ekdal, E.; Akyuz, O.; Can, N. Synthesis and Luminescence Properties of Trivalent Rare-Earth Element-Doped Calcium Stannate Phosphors. *Spectrosc. Lett.* **2014**, *47* (8), 630−641.

(22) Sakthivel, M.; Sukanya, R.; Chen, S. M.; Ho, K. C. Synthesis and Characterization of Samarium-Substituted Molybdenum Diselenide and Its Graphene Oxide Nanohybrid for Enhancing the Selective Sensing of Chloramphenicol in a Milk Sample. *ACS Appl. Mater. Interfaces* **2018**, *10* (35), 29712−29723.

(23) Sukanya, R.; Ramki, S.; Chen, S. M.; Karthik, R. Ultrasound Treated Cerium Oxide/Tin Oxide (CeO_2/SnO_2) Nanocatalyst: A Feasible Approach and Enhanced Electrode Material for Sensing of Anti-Inflammatory Drug 5-Aminosalicylic Acid in Biological Samples. *Anal. Chim. Acta* **2020**, *1096*, 76−88.

(24) Simmons, R. L.; Canafax, D. M.; Fryd, D. S.; Ascher, N. L.; Payne, W. D.; Sutherland, D. E.; Najarian, J. S. New Immunosuppressive Drug Combinations for Mismatched Related and Cadaveric Renal Transplantation. *Transplant Proc.* **1986**, *18*, 76−81.

(25) Shahrokhian, S.; Ghalkhani, M. Glassy Carbon Electrodes Modified with a Film of Nanodiamond-Graphite/Chitosan: Application to the Highly Sensitive Electrochemical Determination of Azathioprine. *Electrochim. Acta* **2010**, *55* (11), 3621−3627.
(26) Asadian, E.; Iraji Zad, A.; Shahrokhian, S. Voltammetric Studies of Azathioprine on the Surface of Graphite Electrode Modified with Graphene Nanosheets Decorated with Ag Nanoparticles. *Mater. Sci. Eng., C* **2016**, *58*, 1098−1104.
(27) Bouhnik, Y.; Lémann, M.; Mary, J. Y.; Scemama, G.; Taï, R.; Matuchansky, C.; Modigliani, R.; Rambaud, J. C. Long-Term Follow-up of Patients with Crohn's Disease Treated with Azathioprine or 6-Mercaptopurine. *Lancet* **1996**, *347* (8996), 215−219.
(28) Fazio, T. T.; Singh, A. K.; Kedor-Hackmann, E. R. M.; Santoro, M. I. R. M. Quantitative Determination and Sampling of Azathioprine Residues for Cleaning Validation in Production Area. *J. Pharm. Biomed. Anal.* **2007**, *43* (4), 1495−1498.
(29) Shafaati, A.; Clark, B. J. Determination of Azathioprine and Its Related Substances by Capillary Zone Electrophoresis and Its Application to Pharmaceutical Dosage Forms Assay. *Drug Dev. Ind. Pharm.* **2000**, *26* (3), 267−273.
(30) Wang, J.; Zhao, P.; Han, S. Direct Determination of Azathioprine in Human Fluids and Pharmaceutical Formulation Using Flow Injection Chemiluminescence Analysis. *J. Chin. Chem. Soc.* **2012**, *59* (2), 239−244.
(31) Göger, N. G.; Parlatan, H. K.; Basan, H.; Berkkan, A.; Özden, T. Quantitative Determination of Azathioprine in Tablets by 1H NMR Spectroscopy. *J. Pharm. Biomed. Anal.* **1999**, *21* (3), 685−689.
(32) Chen, S. P.; Qiao, Z.; Vivoni, A.; Hosten, C. M. Determination of the Orientation of Azathioprine Adsorbed on a Silver Electrode by SERS and Ab Initio Calculations. *Spectrochim. Acta, Part A* **2003**, *59* (12), 2905−2914.
(33) Kong, L.; Karatchevtseva, I.; Blackford, M. G.; Scales, N.; Triani, G. Aqueous Chemical Synthesis of $Ln_2Sn_2O_7$ Pyrochlore-Structured Ceramics. *J. Am. Ceram. Soc.* **2013**, *96* (9), 2994−3000.
(34) Chen, Y. P.; Lin, S. Y.; Sun, R. M.; Wang, A. J.; Zhang, L.; Ma, X.; Feng, J. J. FeCo/FeCoP Encapsulated in N, Mn-Codoped Three-Dimensional Fluffy Porous Carbon Nanostructures as Highly Efficient Bifunctional Electrocatalyst with Multi-Components Synergistic Catalysis for Ultra-Stable Rechargeable Zn-Air Batteries. *J. Colloid Interface Sci.* **2022**, *605*, 451−462.
(35) Dehdari Vais, R.; Sattarahmady, N.; Karimian, K.; Heli, H. Green Electrodeposition of Gold Hierarchical Dendrites of Pyramidal Nanoparticles and Determination of Azathioprine. *Sens. Actuators, B* **2015**, *215*, 113−118.
(36) Shahrokhian, S.; Ghalkhani, M. Electrochemical Study of Azathioprine at Thin Carbon Nanoparticle Composite Film Electrode. *Electrochem. Commun.* **2009**, *11* (7), 1425−1428.
(37) Mei, L. P.; Feng, J. J.; Huang, S. S.; Shi, Y. C.; Wang, A. J. Highly Sensitive Electrochemical Determination of Azathioprine Using a Glassy Carbon Electrode Modified with Au Neuronal-like Nanostructures. *Sens. Actuators, B* **2017**, *240*, 996−1002.

https://doi.org/10.1021/acsanm.1c02591
ACS Appl. Nano Mater. 2021, 4, 13048−13059